Room Temperature AFM Electric Field-Induced Topotactic Transformation Between Perovskite and Brownmillerite $SrFeO_x$ with sub-micron spatial resolution.

Elías Ferreiro-Vila, Santiago Blanco-Canosa, Irene Lucas del Pozo, Hari Babu Vasili, César Magén, Alfonso Ibarra, Juan Rubio-Zuazo, Germán R. Castro, Luis Morellón, Francisco Rivadulla.**

Dr. E. Ferreiro-Vila, Prof. F. Rivadulla
Centro de Investigación en Química Biolóxica e Materiais Moleculares (CIQUS), Departamento de Química-Física, Universidade de Santiago de Compostela, 15782 Santiago de Compostela, Spain.
E-mail: elias.ferreiro@usc.es; f.rivadulla@usc.es

Dr. S. Blanco-Canosa
Donostia International Physics Center (DIPC), 20018, San Sebastián, Spain; IKERBASQUE, Basque Foundation for Science, 48013 Bilbao, Basque Country, Spain.

Dra. I. Lucas del Pozo, Dr. C. Magén, Dr. A. Ibarra, Prof. L. Morellón
Instituto de Nanociencia de Aragón (INA), Universidad de Zaragoza, Departamento de Física de la Materia Condensada, Laboratorio de Microscopías Avanzadas (LMA), and Instituto de Ciencia de Materiales de Aragón (ICMA), Universidad de Zaragoza-CSIC 50018 Zaragoza, Spain.

Dr. H Vasili
ALBA Synchrotron Light Source, Cerdanyola del Valles, 08290 Barcelona, Catalonia, Spain

Dr. J. Rubio-Zuazo, Dr. G. R. Castro
BM25-SpLine Spanish CRG Beamline at the ESRF, 71 Av. Des Martyrs, Grenoble, 38043, France.
Instituto de Ciencia de Materiales de Madrid-CSIC, Sor Juan Ines de la Cruz 3, Cantoblanco, 28049 Madrid, Spain.

Keywords: (thin-films, topotactic reactions, atomic force microscopy)

Abstract.- Reversible structural transformations between perovskite (PV) $ABO_{3-\delta}$ and brownmillerite (BM) $ABO_{2.5}$ ($A=Ca^{2+}$, Sr^{2+}; $B=Fe^{4+/3}$, $Co^{4+/3+}$) oxides can be induced by topotactic oxygen exchange at moderate temperatures under reducing/oxidizing conditions. The combination of a large oxide-ion conductivity and a small free energy difference between the 4+/3+ oxidation states of many 3d transition metal ions enable these topotactic transformations. Herein it is demonstrated that the electric field produced by a voltage-biased Atomic Force Microscopy (AFM) tip can induce such transformation between PV $SrFeO_{3-\delta}$ and BM $SrFeO_{2.5}$

at room temperature, and with sub-micron spatial resolution. Interestingly, the structural transformation is kept after the electric field is removed, allowing a non-volatile control of the local chemical, electrical, optical and magnetic properties. Thus, the results presented in this paper open the door for the fabrication of stable ionic-based devices through the electric field-patterning of different crystallographic phases.

1. Introduction

Oxygen-deficient (Ca,Sr)(Fe,Co)$O_{3-\delta}$ perovskites (PV) exhibit fast O^{2-}-ion mobility and electrical conductivity at high temperature, which make them very appealing for the development of memory devices,[1] and also of solid oxide fuel cells,[2,3] and oxygen separation membranes.[4,5]

On many of these PV, a topotactic oxygen extraction rendering the brownmillerite (BM) (Ca,Sr)(Fe,Co)$O_{2.5}$, or the square-planar (Ca,Sr)(Fe,Co)$O_{2.0}$ can be induced via different chemical/electrochemical reactions,[1,6–11] and high temperature thermal treatments under oxygen/vacuum.[12–19]

But although topotactic transformations (TPt) have been shown to be a powerful tool to tune the properties of several oxides,[20] the need of either high temperatures or specific electrochemical-cell configurations, along with the lack of spatial control over the position and resolution of the transformation, limits its applications in many technologies requiring spatial sub-micron control.

In this work we demonstrate that the TPt between PV and BM phases of $SrFeO_x$ thin films can be induced locally with sub-micron spatial resolution at room temperature by the electric field created by an AFM tip. Accumulation regions of charged oxygen vacancies, $V_{Ö}$, transform spontaneously into the stable BM phase leading to large changes in the electronic and crystal structure of the original perovskite film. Our approach offers important advantages over the previously tested methods to induce the PV-BM transformation, for instance: i) the

crystallographic transformation is achieved at room temperature; ii) the process is performed in ambient conditions, without any further modification of the surface of the film. This is an important advantage over electrochemical methods which require the use of ionic liquids or other electrochemical media, particularly if an additional functionalization of the surface is pursued. Finally, iii) the sub-micrometer spatial control over the crystallographic transformation achieved with this method opens the door to the patterning of stable ionic-based devices with different functionalities.

1. Results and Discussion

Reversible topotactic transformation between the PV and BM phases of $SrFeO_x$ epitaxial thin films can be achieved by post-deposition thermal annealing under different oxygen pressures. In **Figure 1** we show a detail of the X-ray diffraction pattern of a 50 nm thick film of BM $SrFeO_{2.5}$ on a (001) $SrTiO_3$ (STO) substrate. Post-deposition annealing at 500ºC and $P(O_2)$=300 mTorr produces the complete transformation from the orthorhombic BM (a_{pc} =3.97 Å) to the cubic PV phase (a =3.86 Å). A subsequent annealing at the same temperature but under reduced oxygen pressure, $P(O_2)$=0.1 mTorr, results in an oxygen loss from precise positions (topotactic transformation), and the recovery of the BM phase (see the structural model in **Figure 1b**, and **Figure S1** in the supporting information). We verified the occurrence of the transformation in films of $SrFeO_x$ deposited on $SrTiO_3$, $LaAlO_3$, $NdAlO_3$, and MgO, as a proof of the negligible role of the substrate in the PTt transformation. Additionally, X-ray reciprocal space mapping (not shown) demonstrate that the 50 nm films of $SrFeO_x$ on STO remain totally strained, in the BM and PV phases.

On the other hand, although oxygen mobility decreases very rapidly at low temperature, other authors reported that Co/Fe-based perovskites can undergo reversible TPt oxygen uptake to the BM phase at room temperature during electrochemical reactions.[1,6,7,9,21]

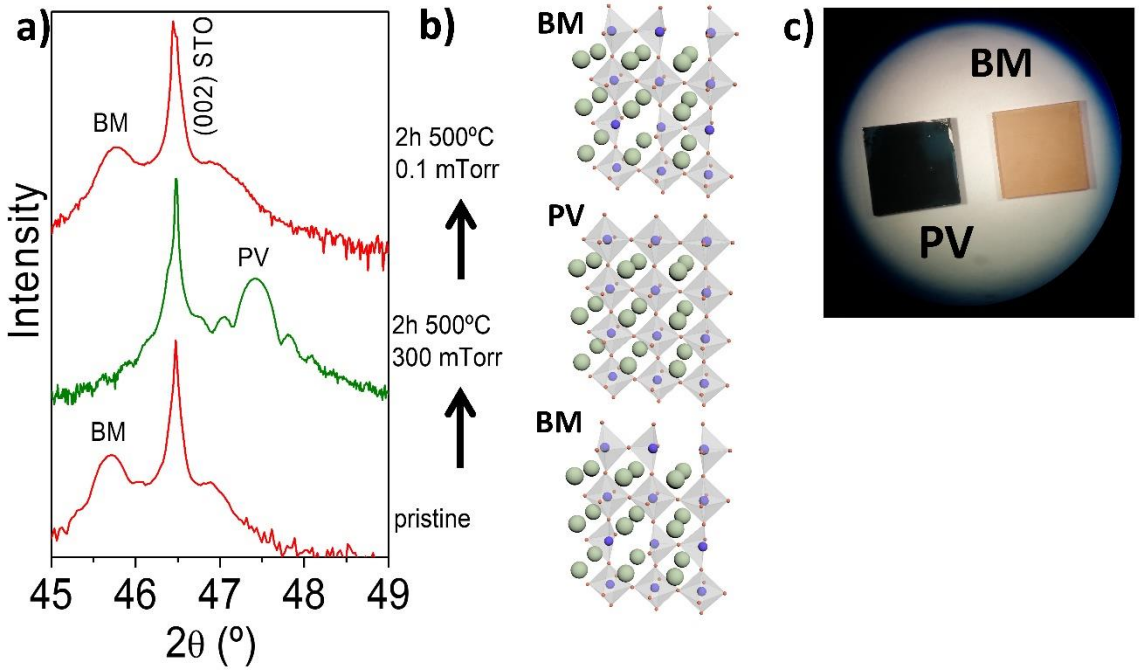

Figure 1. *Bulk topotactic transformation by thermal annealing.* a) Detail of an X-ray diffraction pattern showing the structural transformation between PV $SrFeO_{3-\delta}$ and BM $SrFeO_{2.5}$, for a 50 nm thick film deposited on (001) $SrTiO_3$. The reversible transformation between the PV and the BM is achieved after a post-deposition thermal annealing in 300 mTorr (oxygenation) and 0.1 mTorr (deoxygenation) respectively. b) Schematic representation of the crystal structure of the BM and PV phases. The BM structure exhibits alternating tetrahedral and octahedral layers along one axis, with the oxygen vacancies fully ordered, forming one-dimensional channels along a perpendicular axis. c) Optical image of the BM and of the PV films (5×5 mm^2) after the thermal annealing described in a). The different colors reflect the change from metallic PV to insulating BM.

Therefore, the charged nature of $V_{Ö}$ and their large mobility in the PV phase, should make them amenable to their control by a local electric field applied by a voltage-biased AFM tip, as it was shown in other 3*d*-oxides.[22–25] We hypothesize that the small free energy difference between the PV and BM phases in $SrFeO_x$,[13] could lead to the spontaneous rearrangement of the

vacancies accumulated by the electric field in a region of the PV film, leading to the local transformation into the BM phase.[26]

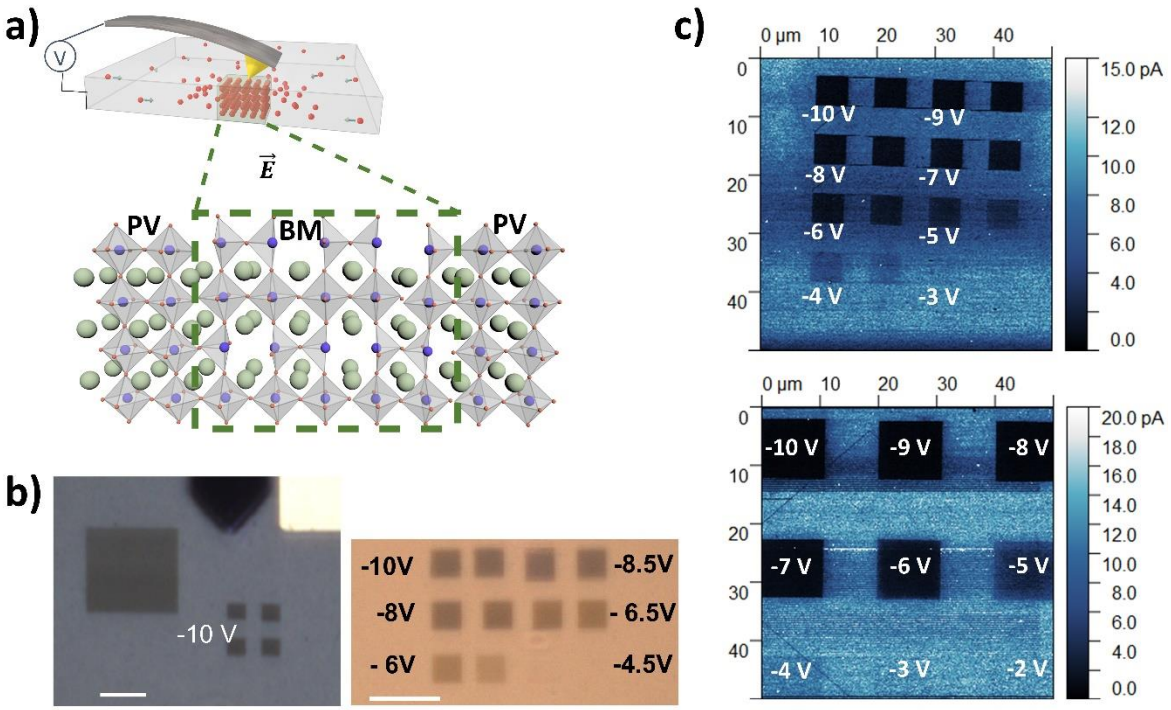

Figure 2. *AFM electric field-induced local topotactic transformation.* a) Applying an electrical voltage between the AFM tip and the PV $SrFeO_{3-\delta}$ film in contact mode produces a large electric field in the region underneath the tip, accumulating $V_{\ddot{O}}$. b) Optical image (taken with the AFM camera, reflected light) of different regions of the film after scanning with -10 V (left). The triangular shadow on the top of the image corresponds to the AFM cantilever. The picture at the right shows different regions scanned with increasing voltages, from - 4.5 V to -10 V, at -0.5 V steps. The areas scanned with the electric field change their color with respect to the conductive PV film background, consistent with a decrease in conductivity. The scale bar is 25 µm long in both images. c) Local electrical conductivity probed by conductive-AFM. The portions of the film previously scanned with the voltage-biased AFM tip become electrically insulating. The conductivity measurements were performed on a $SrFeO_x$ film deposited on a

(001) MgO substrate, to avoid any possible contribution from oxygen vacancies that could be formed in the STO substrate.

Figure 2 a) shows a scheme of this process, in which a negative voltage-biased AFM tip scanning a film of $SrFeO_{3-\delta}$ induces an accumulation region of positively charged $V_{Ö}$. The optical microscope images of **Figure 2 b)** (reflected light) indeed show a clear change in color of an area of the PV $SrFeO_{3-\delta}$ film recorded under a -10 V-biased AFM tip. In this case the darkest accumulation area is consistent with a larger optical bandgap (insulating, no reflecting light), while the surrounding film, not affected by the electric field, remains metallic (intense reflection of light). The change in color is observable in regions scanned above ≈ - 4.5 V, and becomes more intense above ≈ - 7-8 V.

The local electrical conductivity was probed by conductive-AFM. After scanning different portions of the film (of either 10×10 μm^2 or 5×5 μm^2) with a negative biased AFM tip, the local conductivity between the tip and the sample was measured. The results, shown in **Figure 2 c)**, demonstrate a drastic reduction of the electrical conductivity of the regions were $V_{Ö}$ are accumulated by the electric field. This is consistent with the smaller optical reflectance observed in the images and suggests the transformation from conducting $SrFeO_{3-\delta}$ PV to insulating $SrFeO_{2.5}$ BM.

The evolution of the room temperature Raman spectra for different voltages is shown in **Figure 3 a)**. These experiments were performed on a film deposited on LSAT, to avoid the large background signal from STO.[27] The appearance of the peaks at ≈ 331 cm^{-1}, ≈ 430 cm^{-1} and ≈ 625 cm^{-1} in the pristine regions of the film are characteristic of a tetragonal or orthorhombic PV, of composition $SrFeO_x$, x ≈ 2.7-2.9.[28] The intensity of these peaks decreases gradually and shows a blue-shift in the regions scanned with an increasing voltage, at the same time that a broad maximum with a shoulder at ≈ 710 cm^{-1} characteristic of the stretching modes of FeO_4

tetrahedra in the BM phase[29] develops (see **Figure S2** in the supporting information for further details). The comparison with the Raman spectrum of a BM $SrFeO_{2.5}$ film shown in the same figure suggests the full transformation of the PV into BM above ≈ -9 V.

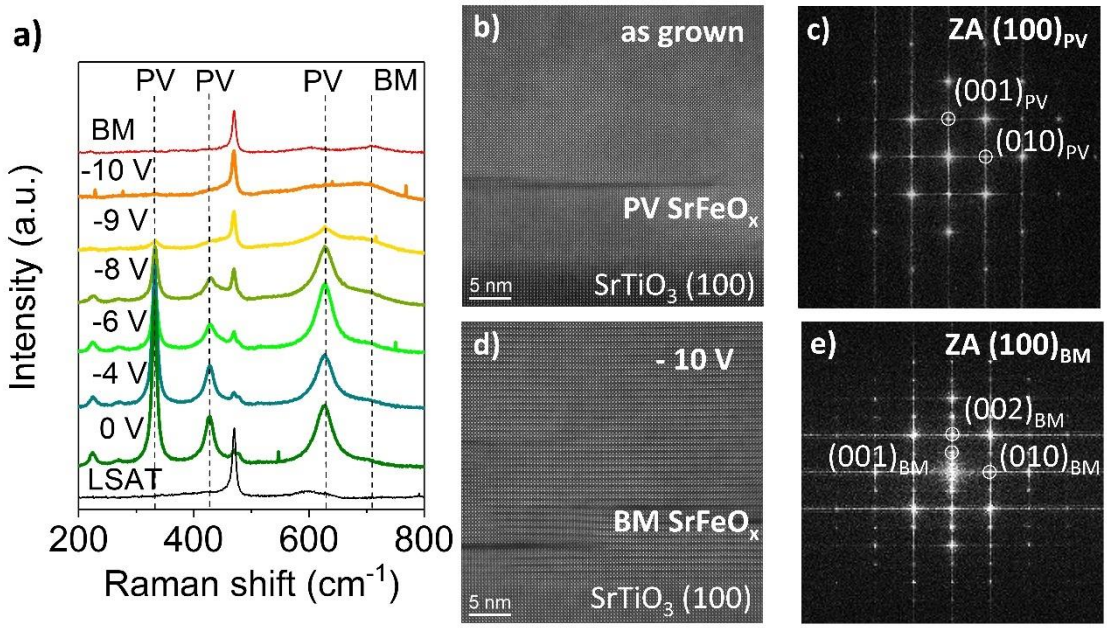

Figure 3. *Structural characterization of the regions scanned by the voltage-biased AFM tip.* a) Room temperature Raman spectra (λ= 532.19 nm) of the PV film after scanning different regions with an increasing voltage. The spectra were displaced vertically for clarity. The Raman spectrum of the substrate (LSAT) and a BM film are also shown for comparison. The peaks characteristic of the PV and BM phase are indicated by vertical dashed lines. The peaks of the PV practically disappear in the regions scanned at the higher voltages, and the broad peak at ≈ 710 cm^{-1} characteristic of the BM appears. b) and c) show the STEM and Fourier transform of a pristine area of the film, showing the microstructure of the PV film. In d) and e) we show the same microstructural analysis of a lamella extracted from an region scanned at -10 V, showing the characteristic morphology and superstructure spots of the BM phase.

The microstructural transformation was corroborated through a comparative scanning transmission electron microscopy (STEM) analysis of two cross-section lamellae; a first specimen extracted from the as-grown area of the sample, and a second specimen extracted from the squared area previously scanned under - 10 V. The as-grown sample evidences a PV pseudo-cubic structure; **Figure 3b)**. This is highlighted by the Fast Fourier Transform (FFT) of the film, **Figure 3c)**, where the main in-plane and out-of-plane periodicities can be indexed as the (001) and (010) reflections of a PV structure. A quantitative analysis of the lattice parameter performed by Geometrical Phase Analysis (GPA)[30] (see **Figure S3** in the Supplementary Information) demonstrates that the film is fully strained, in spite of the presence of sparse structural defects (for instance, stacking faults such as the one clearly visible in the STEM image). The out-of-plane lattice parameter averages 3.83(4) Å, which nicely agrees with the PV lattice parameter deduced from XRD. After the AFM scan at - 10 V, a full transformation of the film has occurred at microscopic level; **Figure 3 d)**. A superstructure characteristic of the BM phase is formed throughout the film increasing the out-of-plane lattice parameter of the original PV structure. This is also reflected in the FFT as an extra spot labeled $(001)_{BM}$ in **Figure 3e)**.[31] As in the parent PV phase, GPA evidences that the film remains strained, and the out-of-plane lattice parameters has expanded up to 3.99(3) Å.

The transformation was additionally characterized through the change in the oxidation state of Fe, by Synchrotron X-ray Absorption Spectroscopy (XAS) around the Fe K and $L_{2,3}$-edges, and the O K-edge, inside and outside an area scanned with a voltage-biased AFM tip (**Figure 4**). An energy shift of at the Fe K-edge to lower energies in the scanned region indicates a lower Fe valence (**Figure 4 a**). According to a calibration curve performed using stoichiometric iron oxides with different oxidation states, the edge displacement increases linearly with the oxidation state (OS) of Fe: $E(eV)= E_0+4.1\times OS$.[32] For the present measurements we have used a Fe foil to extract the E_0=7112 eV. Based on the XAS spectra, we obtained a valence of Fe≈

+3.78 in the pristine region of the film, and Fe≈ + 3.07 in the (150×300 μm^2) area scanned by the - 10 V-biased AFM tip. These values correspond to chemical compositions of $SrFe^{3.78+}O_{2.89}$ and $SrFe^{3.07+}O_{2.54}$, respectively, in agreement with the chemical formula for oxygen deficient PV and BM, respectively.[28] X-Ray Photoemission Spectroscopy (XPS) measurements around Fe 2s energy (see **Figure S4** in the supporting information), led to similar oxidations states: $SrFe^{3.7+}O_{2.85}$ and $SrFe^{3.05+}O_{2.52}$ for the pristine and electric-field scanned region, respectively.

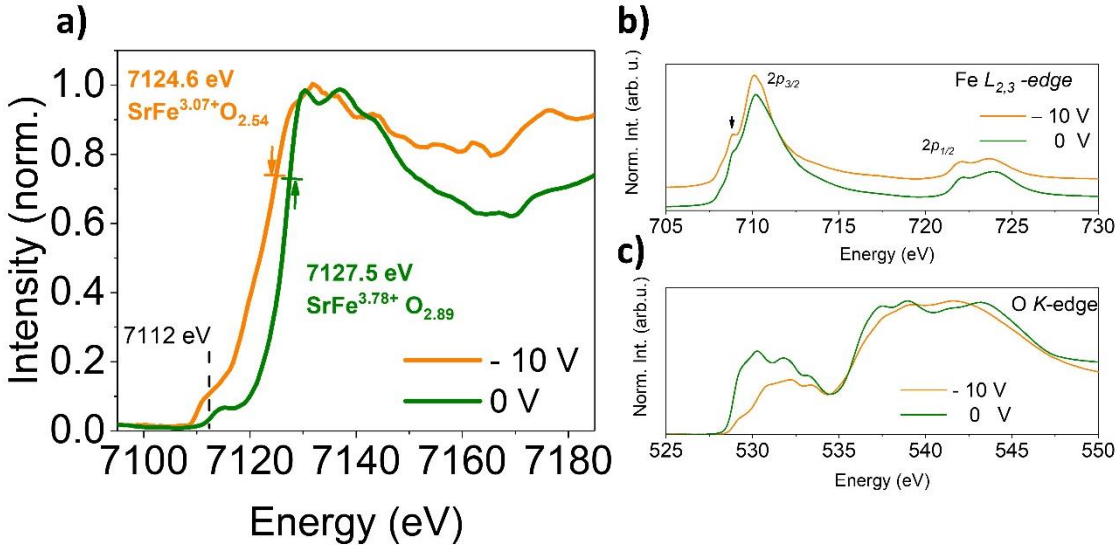

Figure 4. *Spectroscopic evidence of the local PV to BM transformation.* a) Comparison of the Fe K-Edge X-ray absorption on a pristine region of the film (green line), and on an area (150×300 μm^2) previously scanned by the - 10 V-biased AFM tip (orange line). The displacement of the absorption to lower energies in the electric field-scanned region indicates a lower formal charge of Fe (see text). Panels b) and c) show the comparison between the Fe $L_{2,3}$-Edge and O K-Edge X-ray absorption spectra taken on an area scanned with the - 10 V-biased AFM tip (orange line), and a pristine region of the film (green line). The vertical arrow in b) marks a low energy feature in the $2p_{3/2}$ peak, characteristic of a lower Fe-oxidation state and tetrahedral coordination in this region; see text. The spectra were displaced vertically for clarity.

In **Figure 4 b)**, we show the XAS spectra of $SrFeO_x$ around the Fe-$L_{2,3}$-edge, for the pristine PV film and for a region scanned at - 10 V. The isotropic spectra have been obtained as an average of left and right circular polarized light, normalized to maximum intensity of the L_3-edge. The spectra consist of two multiplets (L_3 and L_2) at 710 eV and 722 eV, which are separated by the spin-orbit splitting of the Fe 2p core hole. The peak at the low energy side of the L_3-edge is characteristic of a lower oxidation state of Fe,[33] and it was associated in $SrCoO_{3-\delta}$ to a reduction in the coordination of the transition-metal ion, from octahedral to tetrahedral. The increase of this feature in the region of $SrFeO_{3-\delta}$ scanned with the -10 V-biased AFM tip supports the occurrence of the PV to BM transformation in this area.

The XAS at the O K-edge is shown in **Figure 4 c)**. The peaks between ≈ 528-532 eV result from the transition from O:1s to O:2p states. Previous works demonstrated that PV $SrFeO_{3-\delta}$ is a negative charge transfer system, meaning that the $Fe^{4+/3+}$ redox pair lies below the O^{-}/O^{2-} level.[34–37] In this situation, covalent mixing makes the electronic configuration of $Fe^{4+}(d^4)$ closer to $Fe^{3+}(d^5)$-L, and therefore important information about Fe:3d states can be obtained from the O K-edge adsorption spectrum.[33,38] The crystal field splitting produces the double peak at 530 eV and 532 eV, and its strong suppression after electric field scanning is consistent with an increasing population of tetrahedrally coordinated Fe, as the PV transforms into BM.[39]

Therefore, the microstructural and spectroscopic results discussed so far demonstrate that it is possible to achieve a local, stable topotactic PV-to-BM transformation in thin films of $SrFeO_{3-\delta}$, by the direct action of an electric field-biased AFM tip scanning the bare surface of the film. This strucural tunability is possible by a combination of small $V_{\ddot{O}}$ formation energy in $SrFeO_x$, and a very low free energy difference between the BM and PV phases at room temperature (≈250 meV).[13] These are considerably smaller than for Co or Mn oxides for instance,[14] puting $SrFeO_x$ in an optimal poisition to observe this kind of transformation.

An important result is that, given the considerably larger lattice parameter of the BM (a_{pc}=3.97 Å) with respect to the PV (a=3.86 Å), the crystallographic transformation induced by the AFM tip should be accompanied by a local expansion of the film. Taking the pseudocubic lattice parameters, the full transformation of a 50 nm thick film from PV to BM should increase its thickness by ≈1.2-1.3 nm, perfectly detectable by AFM topography.

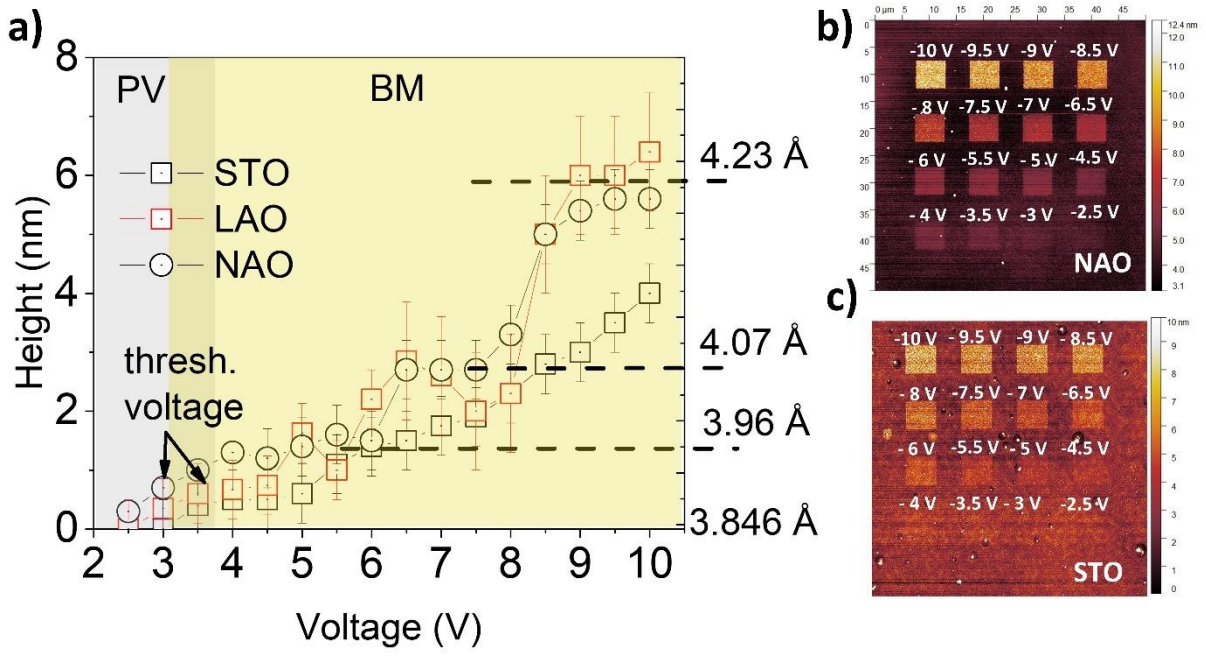

Figure 5. *Topographic effect of the AFM-induced PV to BM transformation.* a) Height of the electric field-scanned regions obtained from the AFM topography, for different applied voltages, and for films deposited on different substrates. The arrows mark the threshold voltage for the transformation. The pseudocubic lattice parameters compatible with such expansion are indicated in the right axis. These were calculated assuming a full transformation of the film. An incomplete tranformation will result in even a larger lattice parameter of the BM lattice. Panels b) and c) show the AFM topography images of the PV $SrFeO_{3-\delta}$ thin films deposited on $NdAlO_3$ (NAO) and STO, respectively, after several squares (5×5 μm^2) have been recorded with an AFM tip biased at different voltages.

In **Figure 5 a)** we show the local increase in height measured by AFM topography of PV $SrFeO_{3-\delta}$ films (50 nm thick) deposited on different substrates, after scanning several areas of $5\times5\ \mu m^2$ with a voltage-biased AFM tip. The AFM images are shown in **Figure 5 b)** and **Figure 5 c)** for films deposited on NAO ($NdAlO_3$) and STO, respectively.

Above a threshold voltage ≈ 2.5-3.5 V, there is a local expansion of the film, reaching a plateau of ≈1.2-1.5 nm between ≈- 4 and - 6 V (Figure 5 a). Although the threshold voltage changes slightly for the films deposited on different substrates, probably reflecting the effect of epitaxial strain in oxygen mobility ($NdAlO_3$, $LaAlO_3$ and $SrTiO_3$ induce a strain on $SrFeO_{3-\delta}$ of ≈-2.5%, ≈-1.8%, and ≈+1.1% respectively),[23] the local expansion induced by the voltage-biased AFM-tip is observed irrespective of the substrate used to grow the $SrFeO_{3-\delta}$ PV film. Also, although $SrTiO_3$ is very susceptible to the creation of oxygen vacancies, $NdAlO_3$, $LaAlO_3$ or MgO, are not.[40,41] Therefore, the observation of the PV-BM transformation in films of PV $SrFeO_{3-\delta}$ on these substrates discards any possible effect of oxygen exchange with the $SrTiO_3$ substrate.

Interestingly, increasing the voltage above ≈ - 7-8 V produces an even larger expansion of the film height, to a maximum of ≈ 4 nm for the films on STO, and of ≈ 5-6 nm for NAO and LAO. This suggests a transformation between different stable intermediate phases, with different oxygen content or microstructure, as previously suggested by other authors.[11,20,42,43] The observation of a larger Raman shift at high voltages also supports this picture (see Figure S2, supporting information).

The expansion observed at high voltages in Figure 5 a) is higher than calculated using the pseudocubic lattice parameters and will require instead $c \approx 4.20$ Å. The local spectroscopic probes discussed before discard the possibility of any material deposition from the tip or oxide segregations to explain the large expansion above ≈- 7 V. Different tips (conductive and insulating) with different force constants were employed in different scanning modes (contact

and non-contact) to discard any possible artifact from electromechanical coupling during the topography measurements.

Also, several areas of 10×10 μm^2 were scanned at -10 V in thin films of PV of different thicknesses, and the local change in height increases linearly with the total film thickness (see **Figure S5** in the supporting information). This confirms the intrinsic nature of the large local expansion observed above ≈- 7 V.

The effect of any possible surface damage by the AFM tip was also verified. Scanning the films with different combinations of bias-voltage and applied force to the AFM tip, demonstrate that the local change from PV to BM is due to the drag of $V_{Ö}$ by the strong, local electric field, and not by an effect of the local pressure or surface damage (**Figure S6** in the supporting information). Additionally, in order to discard any effect coming from the substrate, a bare STO substrate was scanned at -10 V; no change of the surface topography was observed after this process.

Therefore, the large expansion observed at the higher voltages must be characteristic of an intrinsic microstructural or compositional change in the sample. One possibility is a change in the orientation of the oxygen vacancy channels (OVC) of the BM above a certain voltage. A lattice parameter as large as ≈ 4.15 Å was reported in BM $SrFeO_{2.5}$ after a change in the orientation of the OVC from horizontal to vertical.[44] However, this does not seem to be the case in our films, as the STEM analysis shown in Figure 3 b)-e) show OVC parallel to the interface with the substrates in the - 10 V samples.

On the other hand, a large expansion of ≈8 % of the unit cell was reported in $SrCoO_{2.5}$, after H^+ absorption and bonding to the apical O_2^- ions in tetrahedral layers of the BM, to form $HSrCoO_{2.5}$.[1] The dissociation of water from the ambient, in a process in which HO^- ions fill an oxygen vacancy site cannot be excluded in our case.[45] Actually, we followed the evolution of the surface potential of the scanned regions through Kelvin Probe AFM (**Figure S7** in the

supporting information). The observed decay of surface potential could be a result of surface electrochemical activity; ionic species formed from water dissociation at high electric field will produce an accumulation of charge which will decay with time.

In any case, a definitive conclusion about the precise nature of the high-voltage phase requires further microstructural and compositional investigation, beyond the objectives of this paper.

The BM phase formed by the voltage-biased AFM tip at room temperature are perfectly stable over time. **Figure 6 a)-c)** show the AFM topography images and line profiles of 10×10 μm^2 squares just after being recorded at -10 V, and after 5 days under ambient conditions. The changes in topography are negligible during this time, demonstrating an excellent stability of the phases. We have followed some samples over 6 months and found similar results (**Figure S8** in the supporting information).

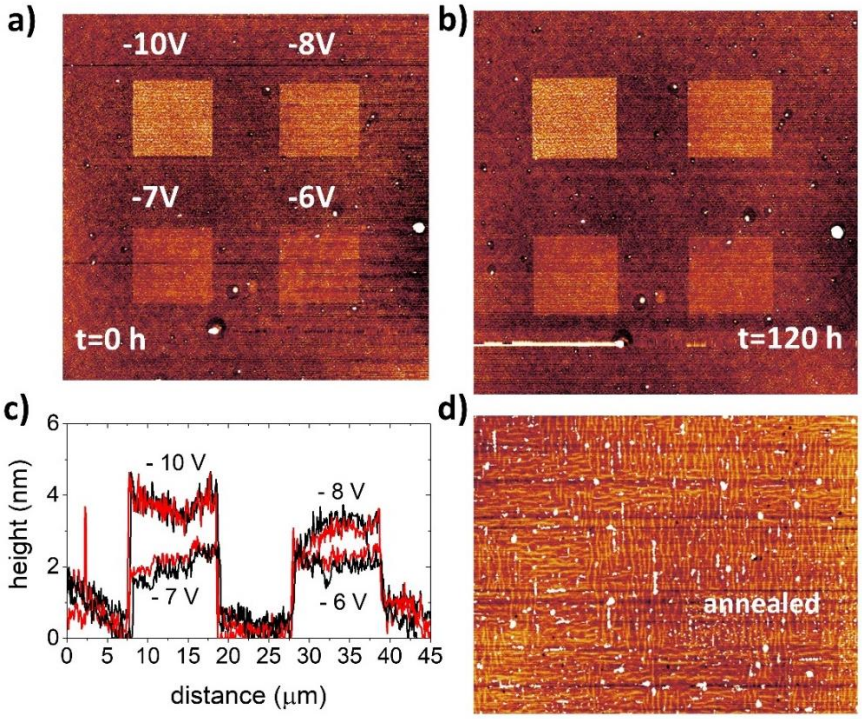

Figure 6. *Stability of the local electric field-induced PV to BM transformation.* Panels a) and b) show the AFM topography of an array of four dots (10×10 μm^2) after being scanned with the AFM tip at different voltages, and after 5 days, respectively. c) Comparison of the topographic

line profile from a) (black line) and from b) (red line). The changes in height after 5 days at room temperature are negligible. d) Topographic image of the area previously recorded after being annealed at 300ºC and 300 mTorr of O_2, demonstrating the thermal reversibility of the effect.

On the other hand, annealing the sample at 300 ºC in 300 mTorr of O_2 for 2 hours is enough to redistribute the $V_{Ö}$ towards the surrounding conducting PV film, or through exchange with the atmosphere.[46] This treatment erases the topographic height (**Figure 6 d**), and recovers the original PV structure in the whole film, demonstrating the thermal reversibility of the effect.

3. Conclusions.

The possibility to control the crystallographic transformation between the PV and BM phases of $SrFeO_x$ at room temperature, using a voltage biased AFM-tip acting directly on the bare surface of the PV film has been demonstrated. This transformation is accompanied by a local expansion of the film thickness and changes in the electrical conductivity, which are stable for months under usual ambient conditions. Given the large difference in the electrical conductivity of the PV and BM, as well as their different magnetic configuration,[47] the local control over the TPt reported in this paper opens enormous possibilities to study, in a controlled way, magnetic exchange interactions at their interface, fabricate stable resistive memories,[48,49] or ionic-conducting circuits, with sub-micrometer resolution (for an example, see **Figure S9** and **Figure S10** in the supporting information). Eliminating the use of ionic liquids or any other electrochemical bath to achieve the transformation at room temperature also offers important advantages over previously reported methods, in terms of undesired reactivity or post-functionalization of the electric field transformed surfaces.

Finally, given the similarities between $SrFeO_x$ and other oxides, like $CaFeO_x$, $(Ca,Sr)CoO_x$, $La_{1-x}Sr_xMnO_3$, or VO_2, susceptible to large changes in their electric, magnetic and structural

properties after oxygen manipulation, the method reported here offers a new approach to design new functional materials.

4. Experimental Section. – Thin films of $SrFeO_{3-\delta}$ were deposited on single-crystal substrates of $SrTiO_3$ (STO), $LaAlO_3$ (LAO), $NdAlO_3$ (NAO) and MgO from a dense ceramic target by Pulsed Laser Deposition (Nd:YAG Laser, λ=266 nm, 5 Hz, fluence ≈1.5 J/cm^2) at a temperature of 700 ºC, and oxygen pressure of $P(O_2)$=10 mTorr. After deposition, the samples were annealed at the growth temperature for 10 min at $P(O_2)=2\times10^{-6}$ Torr to obtain the BM, or at 300 mTorr for the PV. The samples were then rapidly cooled down to room temperature inside the PLD chamber under the same oxygen pressure, to keep the oxygen content.

AFM measurements were performed on a NX10 by Park Systems. All the AFM experiments were performed using Electric Force Microscopy (EFM) mode that allows to apply a bias voltage at the AFM tip, which is electrically conductive (Pt-coated, ≈25 nm tip radius). The surface electric potential of the sample was measured by the Scanning Kelvin Probe mode (SKPM).

High Angle Annular Dark Field Scanning Transmission Electron Microscopy (HAADF-STEM) experiments were carried out in a probe corrected FEI Titan Low Base 60-300. This instrument is equipped with a high brightness field emission gun (X-FEG) and a CETCOR aberration corrector for the probe by CEOS. TEM lamellas for these experiments were prepared in a FEI Dual Beam Nova 200 in cryogenic conditions (-100ºC) to minimize local deoxygenation of the films due to local heating during the milling.

Synchrotron X-ray diffraction and X-ray absorption experiments on the Fe K-edge were performed at the BM25-Spline beamline at the ESRF. The XRD patterns were obtained on a Six-Circle diffractometer in vertical geometry using a photon energy of 15 KeV (λ=0.826 Å) and a beam size of 50 μm x 100 μm (H x V). XAS spectra on the Fe K-edge were acquired in

fluorescence mode using a beam size of 50 μm x 50 μm. Fe $L_{2,3}$ and O K-edges at the BOREAS BL29 beamline at ALBA synchrotron.

The Raman spectra were performed with a Confocal Raman microscope Alpha 300R^+ by WiTec, working in near-backscattering geometry with incident light of wavelength 532.2 nm (1 mW, laser spot around 5 μm diameter, diffraction grating 1800 lines/mm).

Supporting Information.

Supporting Information is available from the Wiley Online Library or from the author. Additional X-ray diffraction, Raman spectrum at different voltages, as well as XPS Fe:3s are provided. AFM images (topography and surface potential) images are shown to demonstrate the stability of the transformation, as well as the minimum size attained and the excellent control over the spatial transformation. GPA analysis of the local lattice parameters of the films in STEM images.

Acknowledgments.- We acknowledge Dra. María Giménez (Inorg. Chem. Department, USC) for discussion and critical reading of the manuscript. This work has received financial support from Ministerio de Economía y Competitividad (Spain) under project No. MAT2016-80762-R, MAT2017-82970-C2-R, PGC2018-101334-A-C22, Xunta de Galicia (Centro singular de investigación de Galicia accreditation 2016-2019, ED431G/09), the European Union (European Regional Development Fund-ERDF) and the European Commission through the Horizon H2020 funding by H2020-MSCA-RISE-2016-Project No. 734187–SPICOLOST. . This project has received funding from the European's Union Horizon 2020 research and innovation programme under grant agreement No. 823717 – ESTEEM3. The microscopy works have been conducted in the Laboratorio de Microscopías Avanzadas (LMA) at Instituto de Nanociencia de Aragón (INA)-Universidad de Zaragoza. Authors acknowledge the LMA-INA for offering access to their instruments and expertise. We also acknowledge the Ministerio de Ciencia, Innovación y Universidades and Consejo Superior de Investigaciones Científicas for provision of synchrotron radiation facilities at BM25-SpLine.

Received: ((will be filled in by the editorial staff))
Revised: ((will be filled in by the editorial staff))
Published online: ((will be filled in by the editorial staff))

References

[1] N. Lu, P. Zhang, Q. Zhang, R. Qiao, Q. He, H.-B. Li, Y. Wang, J. Guo, D. Zhang, Z. Duan, Z. Li, M. Wang, S. Yang, M. Yan, E. Arenholz, S. Zhou, W. Yang, L. Gu, C.-W. Nan, J. Wu, Y. Tokura, P. Yu, *Nature* **2017**, *546*, 124.

[2] A. Chroneos, B. Yildiz, A. Tarancón, D. Parfitt, J. A. Kilner, *Energy Environ. Sci.*

2011, *4*, 2774.

[3] A. J. Fernández-Ropero, J. M. Porras-Vázquez, A. Cabeza, P. R. Slater, D. Marrero-López, E. R. Losilla, *J. Power Sources* **2014**, *249*, 405.

[4] J. F. Vente, S. McIntosh, W. G. Haije, H. J. M. Bouwmeester, *J. Solid State Electrochem.* **2006**, *10*, 581.

[5] J. F. Vente, W. G. Haije, Z. S. Rak, *J. Memb. Sci.* **2006**, *276*, 178.

[6] Q. Lu, Y. Chen, H. Bluhm, B. Yildiz, *J. Phys. Chem. C* **2016**, *120*, 24148.

[7] Q. Lu, B. Yildiz, *Nano Lett.* **2016**, *16*, 1186.

[8] J. Lee, E. Ahn, Y.-S. Seo, Y. Kim, T.-Y. Jeon, J. Cho, I. Lee, H. Jeen, *Phys. Rev. Appl.* **2018**, *10*, 54035.

[9] S. Hu, J. Seidel, *Nanotechnology* **2016**, *27*, 325301.

[10] B. Cui, P. Werner, T. Ma, X. Zhong, Z. Wang, J. M. Taylor, Y. Zhuang, S. S. P. Parkin, *Nat. Commun.* **2018**, *9*, 3055.

[11] A. Maity, R. Dutta, B. Penkala, M. Ceretti, A. Letrouit-Lebranchu, D. Chernyshov, A. Perichon, A. Piovano, A. Bossak, M. Meven, W. Paulus, *J. Phys. D. Appl. Phys.* **2015**, *48*, 504004.

[12] H. Jeen, W. S. Choi, J. W. Freeland, H. Ohta, C. U. Jung, H. N. Lee, *Adv. Mater.* **2013**, *25*, 3651.

[13] A. Khare, D. Shin, T. S. Yoo, M. Kim, T. D. Kang, J. Lee, S. Roh, I.-H. Jung, J. Hwang, S. W. Kim, T. W. Noh, H. Ohta, W. S. Choi, *Adv. Mater.* **2017**, *29*, 1606566.

[14] H. Jeen, W. S. Choi, M. D. Biegalski, C. M. Folkman, I.-C. Tung, D. D. Fong, J. W. Freeland, D. Shin, H. Ohta, M. F. Chisholm, H. N. Lee, *Nat. Mater.* **2013**, *12*, 1057.

[15] Y. Tsujimoto, C. Tassel, N. Hayashi, T. Watanabe, H. Kageyama, K. Yoshimura, M. Takano, M. Ceretti, C. Ritter, W. Paulus, *Nature* **2007**, *450*, 1062.

[16] Y. Shimakawa, S. Inoue, M. Haruta, M. Kawai, K. Matsumoto, A. Sakaiguchi, N. Ichikawa, S. Isoda, H. Kurata, *Cryst. Growth Des.* **2010**, *10*, 4713.

[17] T. Kawakami, Y. Tsujimoto, H. Kageyama, X.-Q. Chen, C. L. Fu, C. Tassel, A. Kitada, S. Suto, K. Hirama, Y. Sekiya, Y. Makino, T. Okada, T. Yagi, N. Hayashi, K. Yoshimura, S. Nasu, R. Podloucky, M. Takano, *Nat. Chem.* **2009**, *1*, 371.

[18] H. J. Kitchen, I. Saratovsky, M. A. Hayward, *Dalt. Trans* **2010**, *39*, 6098.

[19] A. J. Overton, J. L. Best, I. Saratovsky, M. A. Hayward, *Chem. Mater.* **2009**, *21*, 4940.

[20] L. Cao, O. Petracic, P. Zakalek, A. Weber, U. Rücker, J. Schubert, A. Koutsioubas, S. Mattauch, T. Brückel, *Adv. Mater.* **2019**, *31*, 1806183.

[21] M. S. Saleem, B. Cui, C. Song, Y. Sun, Y. Gu, R. Zhang, M. U. Fayaz, X. Zhou, P. Werner, S. S. P. Parkin, F. Pan, *ACS Appl. Mater. Interfaces* **2019**, *11*, 6581.

[22] L. Iglesias, A. Sarantopoulos, C. Magén, F. Rivadulla, *Phys. Rev. B* **2017**.

[23] L. Iglesias, A. Gómez, M. Gich, F. Rivadulla, *ACS Appl. Mater. Interfaces* **2018**, *10*, 35367.

[24] S. Das, B. Wang, Y. Cao, M. Rae Cho, Y. Jae Shin, S. Mo Yang, L. Wang, M. Kim, S. V Kalinin, L.-Q. Chen, T. W. Noh, *Nat. Commun.* **2017**, *8*, 615.

[25] V. R. Nallagatla, T. Heisig, C. Baeumer, V. Feyer, M. Jugovac, G. Zamborlini, C. M. Schneider, R. Waser, M. Kim, C. U. Jung, R. Dittmann, *Adv. Mater.* **2019**, 1903391.

[26] A. Khare, J. Lee, J. Park, G.-Y. Kim, S.-Y. Choi, T. Katase, S. Roh, T. S. Yoo, J. Hwang, H. Ohta, J. Son, W. S. Choi, *ACS Appl. Mater. Interfaces* **2018**, *10*, 4831.

[27] H. W. Jang, A. Kumar, S. Denev, M. D. Biegalski, P. Maksymovych, C. W. Bark, C. T. Nelson, C. M. Folkman, S. H. Baek, N. Balke, C. M. Brooks, D. A. Tenne, D. G. Schlom, L. Q. Chen, X. Q. Pan, S. V. Kalinin, V. Gopalan, C. B. Eom, *Phys. Rev. Lett.* **2010**, *104*, 1.

[28] P. Adler, A. Lebon, V. Damljanović, C. Ulrich, C. Bernhard, A. V. Boris, A. Maljuk, C. T. Lin, B. Keimer, *Phys. Rev. B* **2006**, *73*, 094451.

[29] M. A. Islam, Y. Xie, M. D. Scafetta, S. J. May, J. E. Spanier, *J. Phys. Condens. Matter* **2015**, *27*, 155401.

[30] M. J. Hÿtch, E. Snoeck, R. Kilaas, *Ultramicroscopy* **1998**, *74*, 131.

[31] L. Yao, S. Majumdar, L. Äkäslompolo, S. Inkinen, Q. H. Qin, S. van Dijken, *Adv. Mater.* **2014**, *26*, 2789.

[32] J. Rubio-Zuazo, A. Chainani, M. Taguchi, D. Malterre, A. Serrano, G. R. Castro, *Phys. Rev. B* **2018**, *97*, 235148.

[33] A. S. Harvey, Z. Yang, A. Infortuna, D. Beckel, J. A. Purton, L. J. Gauckler, *J. Phys. Condens. Matter* **2009**, *21*, 015801.

[34] Z. Li, R. Laskowski, T. Iitaka, T. Tohyama, *Phys. Rev. B - Condens. Matter Mater. Phys.* **2012**, *85*, 2.

[35] J. Zaanen, G. A. Sawatzky, J. W. Allen, *Phys. Rev. Lett.* **1985**, *55*, 418.

[36] B. Han, A. Grimaud, L. Giordano, W. T. Hong, O. Diaz-Morales, L. Yueh-Lin, J. Hwang, N. Charles, K. A. Stoerzinger, W. Yang, M. T. M. Koper, Y. Shao-Horn, *J. Phys. Chem. C* **2018**, *122*, 8445.

[37] J. Suntivich, W. T. Hong, Y.-L. Lee, J. M. Rondinelli, W. Yang, J. B. Goodenough, B. Dabrowski, J. W. Freeland, Y. Shao-Horn, *J. Phys. Chem. C* **2014**, *118*, 1856.

[38] M. Abbate, F. M. F. de Groot, J. C. Fuggle, A. Fujimori, O. Strebel, F. Lopez, M. Domke, G. Kaindl, G. A. Sawatzky, M. Takano, Y. Takeda, H. Eisaki, S. Uchida, *Phys. Rev. B* **1992**, *46*, 4511.

[39] L. Karvonen, M. Valkeapää, R.-S. Liu, J.-M. Chen, H. Yamauchi, M. Karppinen, *Chem. Mater.* **2010**, *22*, 70.

[40] C. Mitra, C. Lin, J. Robertson, A. A. Demkov, *Phys. Rev. B* **2012**, *86*, 155105.

[41] A. F. Santander-Syro, O. Copie, T. Kondo, F. Fortuna, S. Pailhès, R. Weht, X. G. Qiu, F. Bertran, A. Nicolaou, A. Taleb-Ibrahimi, P. Le Fèvre, G. Herranz, M. Bibes, N. Reyren, Y. Apertet, P. Lecoeur, A. Barthélémy, M. J. Rozenberg, *Nature* **2011**, *469*, 189.

[42] J. P. Hodges, S. Short, J. D. Jorgensen, X. Xiong, B. Dabrowski, S. M. Mini, C. W.

Kimball, *J. Solid State Chem.* **2000**, *151*, 190.

[43] H. Ikeda, S. Nikata, E. Hirakawa, A. Tsuchida, N. Miura, *Chem. Eng. Sci.* **2016**, *147*, 166.

[44] L. Wang, Z. Yang, M. E. Bowden, Y. Du, *Appl. Phys. Lett.* **2019**, *114*, 231602.

[45] J. H. Yu, J.-S. Lee, J. Maier, *Angew. Chemie Int. Ed.* **2007**, *46*, 8992.

[46] M. Andrä, F. Gunkel, C. Bäumer, C. Xu, R. Dittmann, R. Waser, *Nanoscale* **2015**, *7*, 14351.

[47] B. C. Behera, S. Jana, S. G. Bhat, N. Gauquelin, G. Tripathy, P. S. Anil Kumar, D. Samal, *Phys. Rev. B* **2019**, *99*, 24425.

[48] S. K. Acharya, R. V. Nallagatla, O. Togibasa, B. W. Lee, C. Liu, C. U. Jung, B. H. Park, J.-Y. Park, Y. Cho, D.-W. Kim, J. Jo, D.-H. Kwon, M. Kim, C. S. Hwang, S. C. Chae, *ACS Appl. Mater. Interfaces* **2016**, *8*, 7902.

[49] R. Waser, R. Dittmann, G. Staikov, K. Szot, *Adv. Mater.* **2009**, *21*, 2632.

TOC entry text:

Crystallographic transformation between the conducting perovskite $SrFeO_{3-\delta}$ and insulating brownmillerite $SrFeO_{2.5}$ achieved at room temperature using a voltage biased AFM-tip acting directly on the bare surface of the perovskite film. The method offers a new approach to design new functional materials with sub-micron spatial resolution.

Keyword: AFM Electric-field induced local topotactic transformations

Elías Ferreiro-Vila, Santiago Blanco-Canosa, Irene Lucas del Pozo, Hari Babu Vasili, César Magén, Alfonso Ibarra, Juan Rubio-Zuazo, Germán R. Castro, Luis Morellón, Francisco Rivadulla.**

Room Temperature AFM Electric Field-Induced Topotactic Transformation Between Perovskite and Brownmillerite $SrFeO_x$ with sub-micron spatial resolution.

ToC figure:

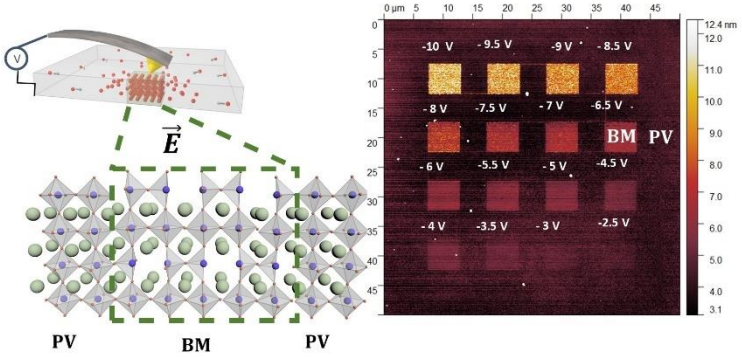

Supporting Information

Room Temperature AFM Electric Field-Induced Topotactic Transformation Between Perovskite and Brownmillerite $SrFeO_x$ with sub-micron spatial resolution.

Elías Ferreiro-Vila, Santiago Blanco-Canosa, Irene Lucas del Pozo, Hari Babu Vasili, César Magén, Alfonso Ibarra, Juan Rubio-Zuazo, Germán R. Castro, Luis Morellón, Francisco Rivadulla.**

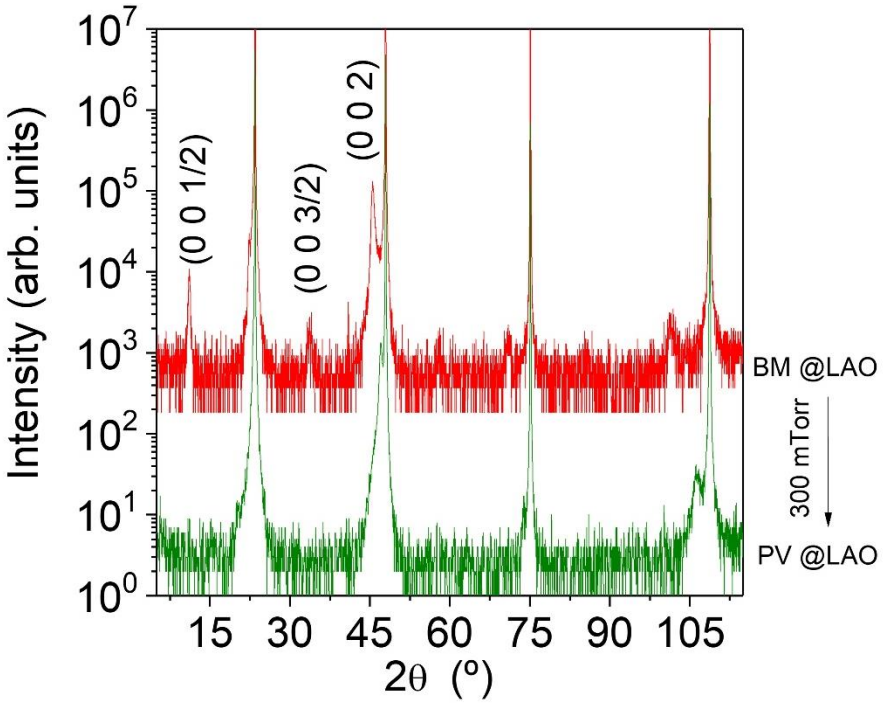

Figure S1. *Topotactic transformation by thermal oxygen annealing of the thin films.* Full X-ray diffraction pattern of a 50 nm thick BM $SrFeO_{2.5}$ film deposited on (001) LAO (at 0.1 mTorr), before (top) and after (bottom) a thermal annealing at 300 mTorr to promote the transformation to PV $SrFeO_{3-\delta}$. The more intense half-order reflections characteristic of the oxygen vacancy ordering in the BM film are indicated.

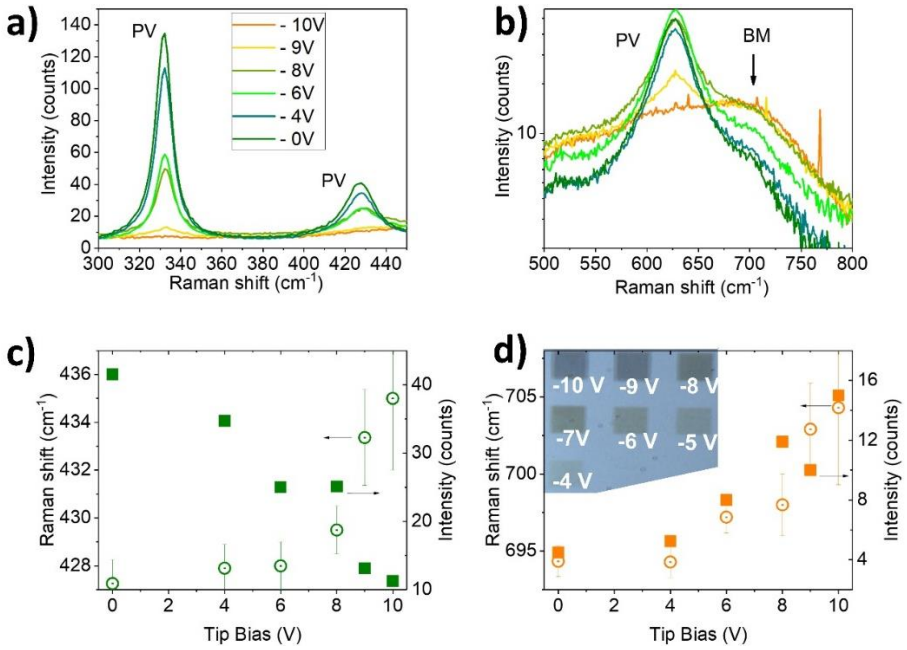

Figure S2. *Raman characterization of the structural transformation.* Panels a) and b) show a detail of the Raman spectrum around several peaks characteristic of the PV and BM phase, as a function of the voltage bias applied to the AFM tip. The intensity of the peaks associated to the PV (BM) phase decrease (increase), as the voltage bias increases. The evolution of the Raman shift and intensity of a peak characteristic of the PV and BM are shown in c) and d), respectively. The evolution of the Raman shift suggest the existence of an intermediate phase between ≈ 4-8 V, and a faster transformation beyond this voltage. An optical image of the different regions probed by Raman is shown in the inset to panel d).

Quantitative analysis of the HAADF-STEM images was performed by Geometrical Phase Analysis (GPA) in order to determine the local variations of the lattice parameter of the as-grown PV and the BM phase induced by the voltage-biased AFM scan. These results are illustrated in Fig. S3. The films are fully strained, with in plane lattice parameter of both PV and BM flms virtually the same (-0.4% in PV, -0.7% in BM), except where stacking faults are present. The out-of-plane deformation with respect to the substrate averages -1.0% in PV and +2.3% in BM.

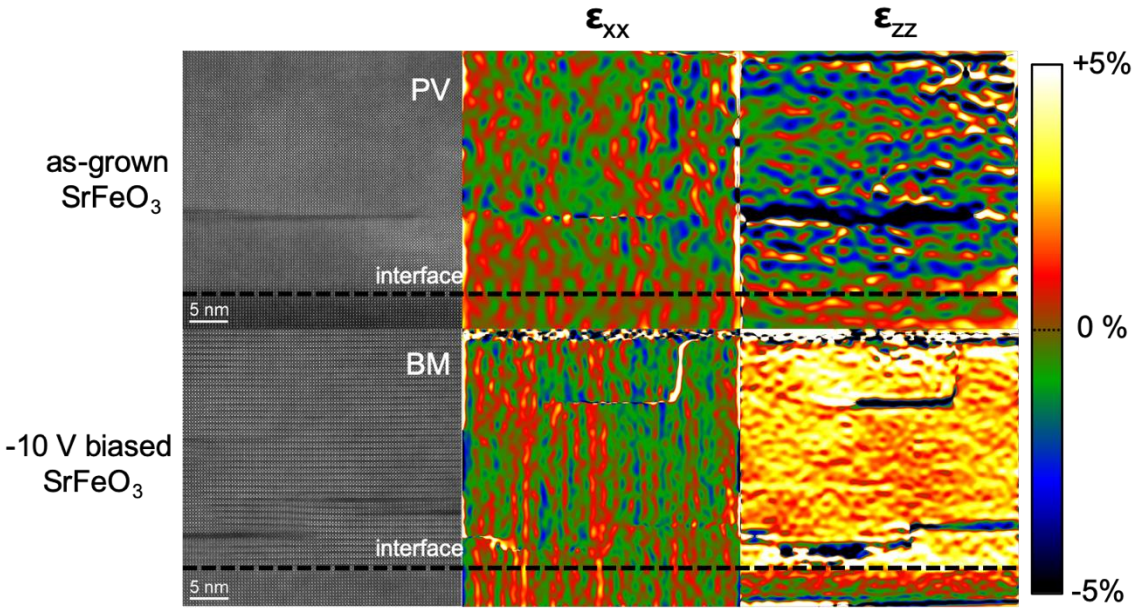

Figure S3. GPA analysis of the HAADF-STEM images of the PV phase (top row) and the BM phase (bottom row). It includes the in-plane (ε_{xx}, central column) and out-of-plane (ε_{zz}, right column) lattice deformation with respect to the substrate.

X-ray Photoemission Spectroscopy (XPS) experiments were performed at the SpLine Spanish CRG Beamline at the ESRF. The oxidation state of Fe can be determined from the energy distance between the two peaks of the spectrum.[[50]] The energy difference is consistent with an Fe valence ≈ +3.7 ($SrFe^{3.7+}O_{2.85}$) in the pristine region and ≈ +3.05 ($SrFe^{3.05+}O_{2.52}$) in the region scanned with an electric field; Figure S4. These results are very similar to those obtained from X-ray absorption, demonstrating the full transformation between the PV and BM phases in the electric field-polarized regions.

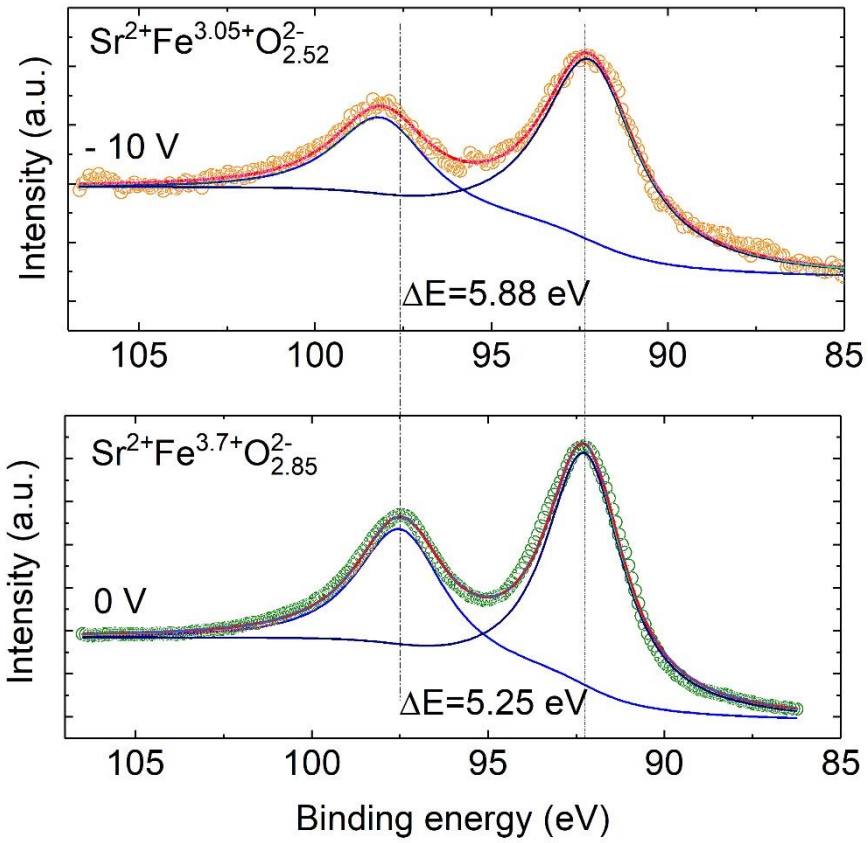

Figure S4. *X-ray Photoemission Spectroscopy (XPS) of the local PV to BM transformation.* The comparison of the Fe: 3s X-ray photoemission spectrm between the pristine and polarized regions is shown in b) and c), respectively. The oxidation state of Fe can be determined from the energy distance between both peaks.

To verify that the PV to BM transformation occurs across the whole thickness of the films, from surface to the interface with the substrate, we have grown $SrFeO_{3-\delta}$ films of different thicknesses (10, 15, 30 and 50 nm) on top of $SrTiO_3$ substrates, and scanned regions of 10×10 μm^2 with an AFM tip biased at -10 V. The local increase of height after the electric field scan was measured by AFM topography. As shown in Figure S5, the increase in height created by the electric field increases linearly with the film thickness, suggesting a full transformation from the surface to the interface with the substrate.

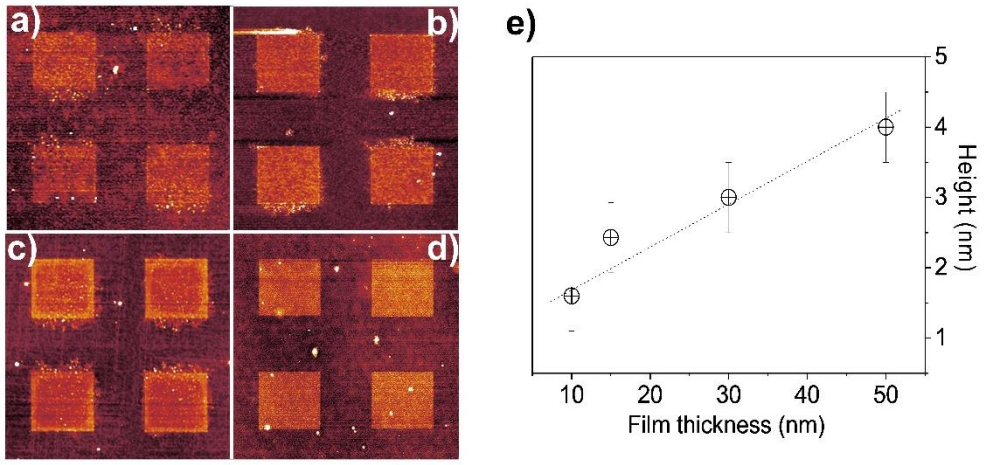

Figure S5. Electric field-induced increase of height as a function of film thickness. AFM topography images of four 10x10 μm^2 regions scanned at -10 V. The pictures from a) to d) correspond to films of 10, 15, 30 and 50 nm thick, respectively. e) Increase of the local height after the electric field PV to BM transformation for different film thicknesses.

We have also verified that the local increase of the topography is not due to a damage of the surface by the AFM tip. We have scanned different regions of the films varying the force applied by the AFM tip, as well as the voltage. Figure S6 a) shows an optical microscope image of three sets of four 10×10 μm^2 squares using different parameters for the applied voltage and force. While it is possible to induce the PV to BM transformation with no applied force under -10V, using force (150 nN for instance) with 0 V results in a negligible change in the local topography.

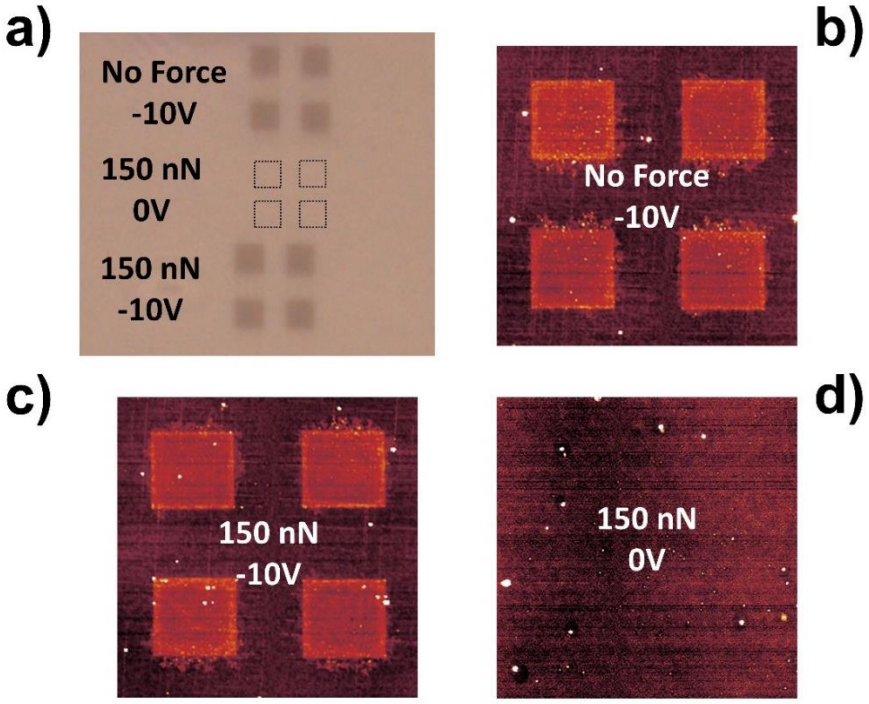

Figure S6. *Effect of force and voltage.* a) Optical microscope image of a four 10×10 μm^2 square scanned at -10 V with no force applied during the AFM scan (top array), at zero voltage with a force of 150 nN during the scan (middle array) and at -10 V with a force of 150 nN (bottom array). b)-d)AFM topography images of the respective arrays (all presented with the same color scale).

The accumulation of $V_Ö$, and the lower conductivity of the BM phase, results in an increase of the surface potential of the area scanned with the AFM-biased tip (Figure S7). Interestingly, although the topography does not change with time, the surface potential decreases continuously.

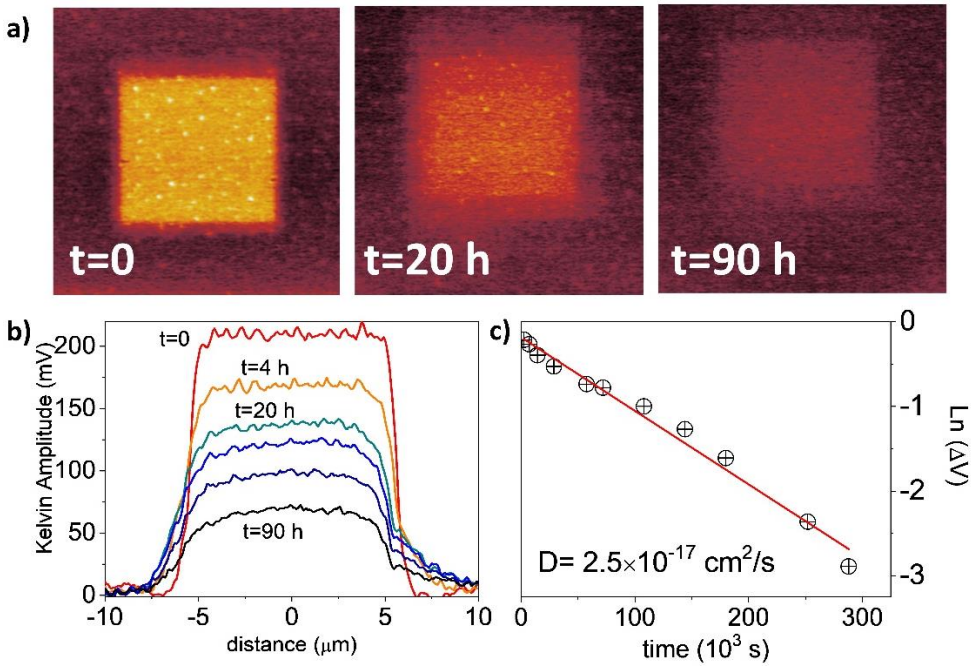

Figure S7. Kelvin probe AFM images taken at different times to show the temporal evolution of the surface potential of an area previously polarized at - 4 V. b) Line profile of the surface potential at different times. c) Fitting of the surface potentail to the difussion equation.

There is a rapid decrease of the KPFM signal after removal of the electric field. The solution of the Fick's diffusion equation along the film-thickness, L, leads to the following time decay of the surface potential:[2]

$$\frac{V(t)-V(t=\infty)}{V(t=0)} \approx \frac{8}{\pi^2} e^{\frac{-\pi^2 Dt}{l^2}}$$

Fitting the data of Figure 6 b) to this equation, taking 90 h as infinite time, leads to D=2.5×10^{-17} cm^2/s.

The observed decay of surface potential measured by KPFM could be a result of the electrochemical activity, since at high electric field, ionic species formed from water dissociation (which produce an accumulation of charge) will decay in time.

The stability of the samples under ambient conditions was followed during a long period of time. Figure S8 shows the AFM topography of two samples scanned with a difference of approximately six months.

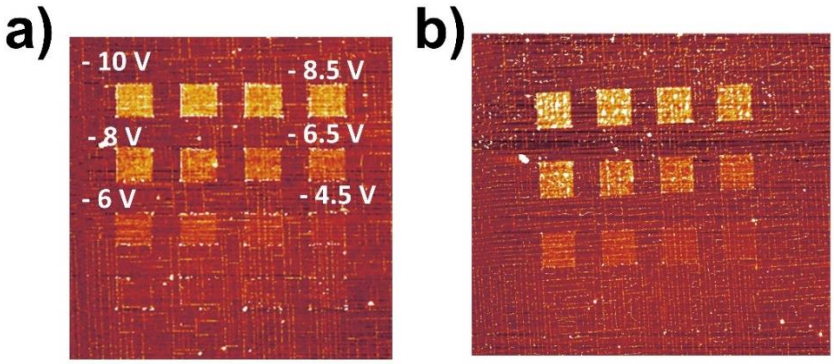

Figure S8. Stability of the crystallographic transformation. a) AFM image of a film after scanning several 10×10 μm^2 square regions with different voltages. b) the same area scanned after six months.

The minimum size attainable in our setup is of the order of 100×100 nm^2 square; see Figure S9.

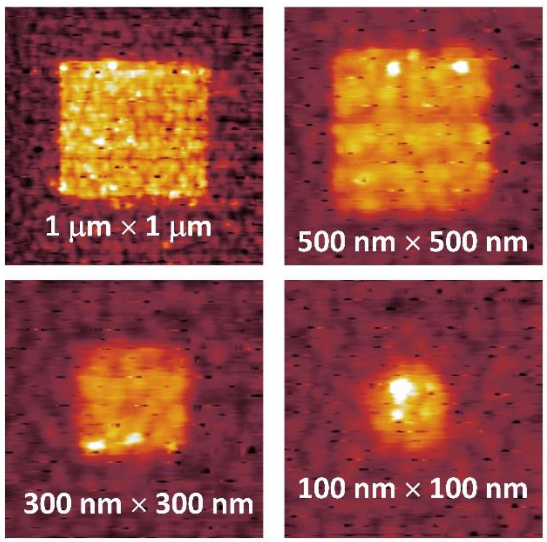

Figure S9. AFM topography images of squares of BM of different sizes, written at - 7 V.

The stability of the transformation offers enormous possibilities to design circuits and patterns with different properties. In Figure S10 we show an example of three letters written in micron-size scale.

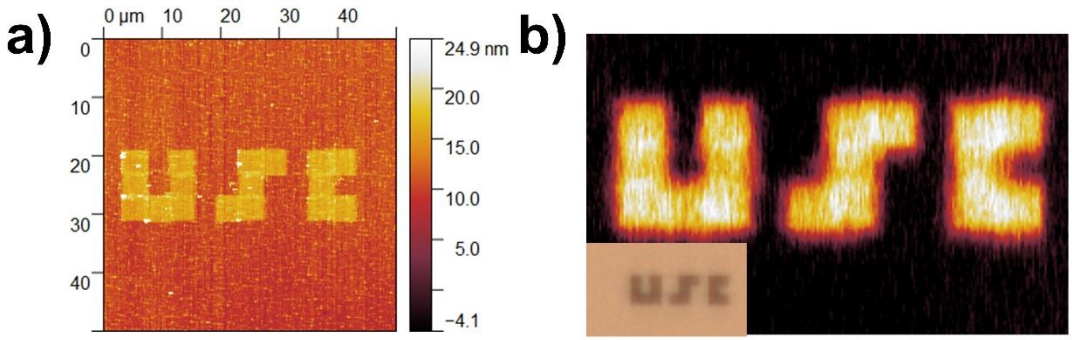

Figure S10. a) AFM topography and Kelvin probe (surface potential) AFM image b) of the word USC (inset: optical microscope image).

REFERENCES

(1) V. R. Galakhov, E. Z. Kurmaev, K. Kuepper, M. Neumann, J. A. McLeod, A. Moewes, I. A. Leonidov, V. L. Kozhevnikov, J. Phys. Chem. C **2010**, 114, 5154.

(2) L. Iglesias, A. Gómez, M. Gich, F. Rivadulla, ACS Appl. Mater. Interfaces **2018**, 10, 35367.